OPTICA

# Large reconfigurable quantum circuits with SPAD arrays and multimode fibers

Adrian Makowski,[1,2] Michał Dąbrowski,[1,3,4] Ivan Michel Antolovic,[5,6] Claudio Bruschini,[5] Hugo Defienne,[7] Edoardo Charbon,[5] Radek Lapkiewicz,[2] and Sylvain Gigan[1,*]

[1]Laboratoire Kastler Brossel, ENS-PSL Université, CNRS, Sorbonne Université, Collège de France, 24 rue Lhomond, Paris 75005, France
[2]Institute of Experimental Physics, Faculty of Physics, University of Warsaw, Pasteura 5, 02-093 Warsaw, Poland
[3]International Centre for Translational Eye Research, Skierniewicka 10A, 01-230 Warsaw, Poland
[4]Institute of Physical Chemistry, Polish Academy of Sciences, Kasprzaka 44/52, 01-224 Warsaw, Poland
[5]School of Engineering, École polytechnique fédérale de Lausanne (EPFL), Rue de la Maladière, Neuchâtel CH-2002, Switzerland
[6]Pi Imaging Technology SA, 1015 Lausanne, Switzerland
[7]Sorbonne Université, CNRS, Institut des NanoSciences de Paris, INSP, Paris F-75005, France
*sylvain.gigan@lkb.ens.fr

Received 27 September 2023; revised 20 December 2023; accepted 20 December 2023; published 28 February 2024

**Reprogrammable integrated optics provides a natural platform for tunable quantum photonic circuits, but faces challenges when high dimensions and high connectivity are involved. Here, we implement high-dimensional linear transformations on spatial modes of photons using wavefront shaping together with mode mixing in a multimode fiber, and measure photon correlations using a time-tagging single-photon avalanche diode (SPAD) array. Our demonstration of a generalization of a Hong-Ou-Mandel interference to 22 output ports shows the scalability potential of wavefront shaping in complex media in conjunction with SPAD arrays for implementing high-dimensional reconfigurable quantum circuits. Specifically, we achieved (80.5 ± 6.8)% similarity for indistinguishable photon pairs and (84.9 ± 7.0)% similarity for distinguishable photon pairs using 22 detectors and random circuits.** © 2024 Optica Publishing Group under the terms of the Optica Open Access Publishing Agreement

https://doi.org/10.1364/OPTICA.506943

Quantum optics with indistinguishable photons has emerged as a key resource in advancing quantum information processing, communication, and metrology, owing to its unique properties such as entanglement, superposition, and non-locality [1–3]. One area of interest is the study of photonic quantum walks, which explores the behavior of quantum particles in complex environments [4,5], with applications in quantum simulations, communication, and sensing [6–8]. Several groups have made remarkable strides in the development of quantum walk, including the first realization of 2D quantum walks on a lattice [9], a quantum walk in a 21-waveguide array [10], and the studies of bound states between systems with different topologies [11].

However, these experimental setups have stringent limitations regarding reprogrammability and scalability due to the integration of detection technology [12], which are crucial for scaling the system to a higher number of modes for implementation on near-term quantum devices. This required a large number of detectors, rendering the solution of problems like boson sampling [13] challenging. Several experiments have employed single-outcome projective measurements for sequential analysis of the output state [5]. However, these approaches suffer from inherent limitations, including substantial losses (as only two outputs can be detected simultaneously) and time-intensive procedures (scaling exponentially with photon numbers). Overcoming these issues is crucial for performing multidimensional unitary operations on the single photons efficiently [14].

In this Letter, we present a reprogrammable and scalable platform for implementing the quantum walk of a two-photon state using a multimode fiber (MMF) as a quantum state mixer [12,14,15]. Our platform generates an arbitrary N-output × 2-input quantum state operation that can be reprogrammed on demand at a 10 Hz frequency rate (see Fig. 1). This provides significant advantages over existing experimental setups [16,17] and makes it a promising candidate for the future realizations of highly multimode quantum walk experiments [9,18]. The wavefronts of the photons are shaped using a spatial light modulator (SLM), and then coupled into MMF supporting around 400 modes at wavelength $\lambda = 800$ nm with low losses [12]. The ability to modify the phase pattern on the SLM allows the MMF to performs a specific linear operation on a two-photon state. This operation can be easily and reliably adjusted on demand. We use a 23-single-photon avalanche diode (SPAD23) [19] array to demonstrate system programmability and investigate scalability up to 22 spatial modes.

Degenerate photon pairs at 810 nm are produced by a type-II spontaneous parametric down conversion (SPDC) process in a ppKTP crystal pumped by a 405 nm continuous wave laser. To split the photons with orthogonal polarizations, we use a polarization beam splitter (PBS). Our SPDC setup allows us to adjust the time delay between the photons, and then observe and control Hong-Ou-Mandel (HOM) interference [20] by changing the

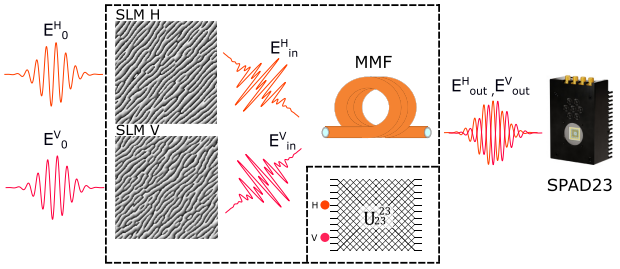


**Fig. 1.** Reprogrammable and scalable platform for quantum operations on a two-photon state. Wavefronts of two photons, generated using SPDC process, are shaped using two separate parts of the SLM before being coupled into MMF used as a quantum states mixer. SPAD23 detector [16] enables for subset $\mathcal{L}_2^{23}$ arbitrary 23-output × 2-input quantum state operations of the general $\mathcal{U}_{23}^{23}$ unitary transformation performed by MMF.

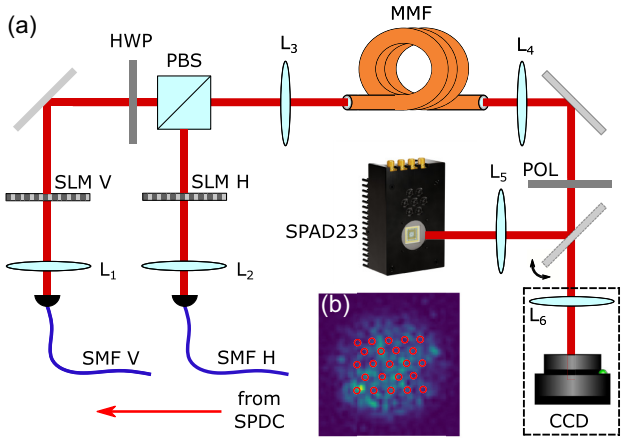


**Fig. 2.** Experimental setup. (a) Orthogonally polarized ($H$ and $V$) photons are wavefront-shaped by the SLM (calibrated by TM measurement) and then coupled into MMF whose output is imaged on the SPAD23 or CCD by changing the flip-mirror position to measure the number of counts and coincidences. (b) CCD speckle image of the light coming out of the MMF with marked SPAD23 detector positions obtained by focusing light through the MMF onto each individual detector.

photons' distinguishability. The measured HOM visibility of photons from our SPDC source is approx. 95% (Supplement 1).

In our experiment, we utilized a detector array consisting of single-photon avalanche diodes (SPADs) using CMOS technology [21,22], specifically the SPAD23 model from Pi Imaging Technology [19]. This detector offers a sub-ns temporal resolution (120 ps jitter FWHM and 20 ps for least-significant bit when using time-to-digital converters as time-taggers). It exhibits low dark noise, with each used detector in the SPAD array having less than 100 counts per second at 20°C. Additionally, the SPAD array with added microlenses has a high pixel fill factor (80%), and a "dead time" of approximately 50 ns [23], which applies to each individual detector in the SPAD array.

Figure 2 depicts the experimental setup used in our study. Two separate parts of the spatial light modulator (SLM), labeled as $H$ and $V$ for orthogonal light polarizations, were illuminated with two photons created in our SPDC platform. The SLM shaped the wavefronts of the photons, which were then focused on the MMF of 50 μm core diameter. The MMF with SLM induces a specific quantum operation on a two-photon state, and modifying the phase pattern on the SLM allows for easy adjustment of this operation. The resulting speckle image of the light emerging from the MMF was either imaged on the SPAD23 or the CCD camera after passing through a polarizer to choose just one particular polarization (for which the TM was measured). To calibrate the relative position of the MMF and SPAD23, we used a CCD camera [Fig. 2(b)]. The positions of the SPAD detectors were accomplished by focusing light through the MMF onto each individual detector (Supplement 1) with magnification chosen to map one speckle mode of the MMF into a single SPAD detector. The photon arrival time was measured using the SPAD23 detector and then used to calculate the number of counts $n_i$ for each detector $i$ and coincidences $C_{ij} = \langle n_i n_j \rangle_t$ for each pair $(i,\ j)$.

Our platform establishes a connection between input modes displayed on the SLM and corresponding output modes measured using 23 detectors described by unitary operator $\mathcal{U}_{23}^{23}$, via well-established transmission matrix (TM) measurement of the optical system [24]. The measured TM remains valid for a few days in normal laboratory conditions. We measure TM in a Fourier mode basis by displaying phase ramps on the SLM with a varying inclination and orientation [25]. This allows us to scan the different spatial positions at the entrance of the MMF and as a result to address particular output modes of the MMF after TM calibration. If the addressed mode is not an eigenvector of the TM, the light becomes scrambled as it propagates through the MMF. The EM field amplitude at SPAD23 is linearly dependent on the EM field on SLM and can be represented as $E_{\text{out}}^{(k)} = T_k^{(1)} E_{\text{in}}^{(k)}$, for $k = H,\ V$, where $E_{\text{out}}^{(k)}$ is the electric field at SPAD23, $T_k^{(1)}$ is a one-photon TM for SLM part $k$, and $E_{\text{in}}^{(k)}$ is the EM field corresponding to the SLM part shaping the polarization $k = H,\ V$. We perform this operation separately for both light polarizations (SLM parts) and then calculate the transmission matrix for the two-photon state $T_H^{(1)},\ T_V^{(1)} \rightarrow T^{(2)}$ [14].

We can readily calculate the SLM pattern that gives us the required quantum operation on the two-photon state $\mathcal{L} \in \mathbb{M}_{2\times N}$, where $N$ is the number of detectors. The computation of the SLM pattern for a given $\mathcal{L}$ takes only a few seconds. The electric field on SLM can be calculated using the complex conjugate of the transmission matrix for the two-photon state $[E_{\text{in}}^{(H)},\ E_{\text{in}}^{(V)}] = T^{\dagger(2)}\mathcal{L}$. Knowing the TM of the MMF, one can modify the phase pattern at the speed of 10 Hz on the SLM and obtain different $N$-output × 2-input linear network operations $\mathcal{L}_2^N$.

As an example of an all-to-all operator, we emulate a 2 × 10 linear network operator of full 10 × 10 Sylvester operation [12] on the two-photon state generated by the experimental platform described above. We measured the TM of the MMF in our setup to calculate the appropriate SLM pattern for performing the 10-dimensional Sylvester operation $\mathcal{L}_S = 1$ for $k = V$ and $\mathcal{L}_S = (-1)^i$ for $k = H$, where $i$ denotes the detector index. We measured the number of coincidence counts for distinguishable and indistinguishable photon pairs.

Figure 3(a) shows a Hong-Ou-Mandel (HOM) interference scan for a four-dimensional Sylvester operator, which corresponds to the number of coincidences as a function of the relative delay between the two photons. The HOM dip in the scan indicates the presence of interference between the two photons, which is essential for quantum operations with indistinguishable particles [20]. The HOM visibility $V$ for different coincidence distributions $C_{i,j}$, ranging from $V = 0.74$ to $V = 0.92$, deviates from ideal (95% visibility of the source) mainly because of cross-talk between different

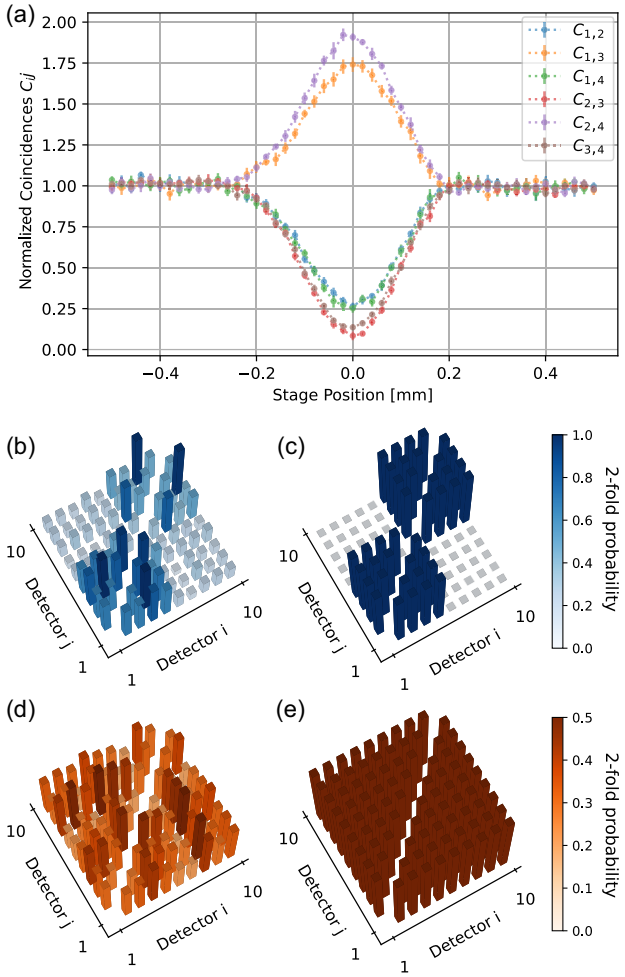


**Fig. 3.** Two-photon interference experimental results. (a) HOM interference for all possible $2 \times 4$ subsets of full $4 \times 4$ operation as a function of the relative delay between photons (error bars-standard deviations). (b)–(e) Example results of a $2 \times 10$ operation on the two-photon state. Panels (b) and (c) [(d) and (e)] show the experimental (b)[(d)] and theoretical (c)[(e)] coincidence counts for indistinguishable [distinguishable] photon pairs, respectively, acquired over a 100 s measurement period.

SPAD23 detectors (Supplement 1) as well as photons' spectral dispersion when propagating through the MMF and non-perfect fidelity of the linear network operator.

Figures 3(b) and 3(d) show the experimental coincidence counts for indistinguishable and distinguishable photon pairs, respectively, over 10 output modes. These counts were acquired for 100 s by measuring the number of coincidences between the SPAD23 detectors with either indistinguishable or distinguishable photons. The theoretical coincidence counts for indistinguishable and distinguishable photon pairs [26] are presented in Fig. 3(c) and 3(e), respectively. As compared with the experimental results presented in Figs. 3(b) and 3(d) we see they agree well with the theoretical predictions [26]. This demonstrates that our experimental platform can successfully generate two-photon states for quantum operations, as well as we can measure and characterize their properties through coincidence counting.

Finally we have checked the scalability and reprogrammable nature of our experimental platform by performing random matrix quantum operations with varying numbers of detectors. Figure 4(a) presents coincidence distributions derived through multidimensional Sylvester operation [12], which we determined

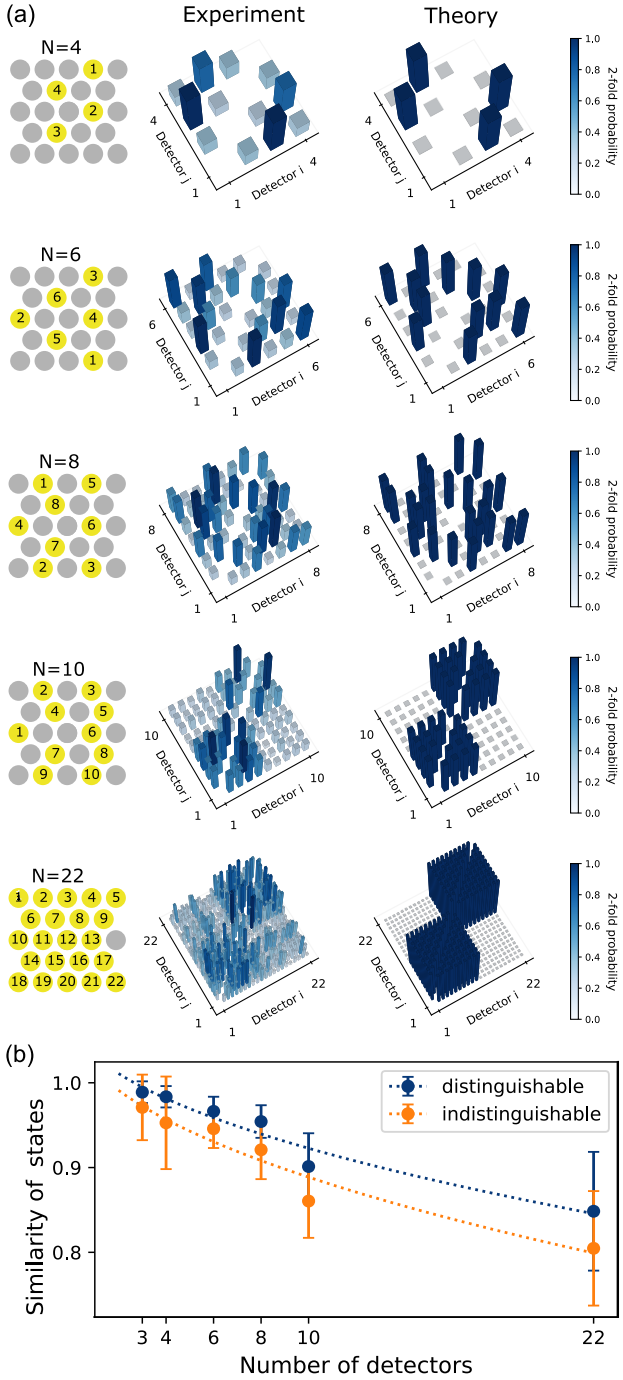


**Fig. 4.** Scalability demonstration. (a) Sylvester transformation for different numbers of detectors: SPAD23 detectors being used (yellow), experimental coincidence counts for indistinguishable photon pairs, and corresponding theoretical coincidence counts (min-max ratio on each plot is around three). (b) Random operation similarity trend for indistinguishable and distinguishable photon pairs (error bars-standard deviations). Fitted curves based on Supplementary Information of [12].

by measuring the number of coincidences between the desired numbers of SPAD detectors. One of the detectors with the highest number of dark counts was excluded from the experiments.

Figure 4(b) shows the difference between the similarity trend for distinguishable and indistinguishable photon pairs $\langle \mathcal{S}_{ET} \rangle_{\mathcal{L}_R}$ when performing 100 random $\mathcal{L}_R$ operations (random complex numbers from a uniform distribution) for different numbers of

used SPAD detectors. The similarity $\mathcal{S}_{ET}$ of two coincidence distributions, experimental $C_{i,j}^{(E)}$ and theoretical $C_{i,j}^{(T)}$ (corresponding to particular $\mathcal{L}_R$ operator), representing a generalized fidelity for two-fold coincidences [10], is defined as

$$\mathcal{S}_{ET} = \frac{\left(\sum_{i,j} \sqrt{C_{i,j}^{(E)} C_{i,j}^{(T)}}\right)^2}{\sum_{i,j} C_{i,j}^{(E)} \sum_{i,j} C_{i,j}^{(T)}}, \tag{1}$$

where $i$ and $j$ denote detectors used for the operation. In other words, similarity quantifies the extent to which the experimental results align with theoretical predictions, with higher values indicating stronger agreement. We see that the similarity decreases as we increase the number of detectors from four to 22, from $98.3 \pm 1.23\%$ ($95.3 \pm 5.5\%$) to $84.9 \pm 7.0\%$ ($80.5 \pm 6.8\%$) for distinguishable (resp. indistinguishable) photons. The similarity is higher for distinguishable pairs because of more stringent conditions for two-photon interference (distinguishable photons are not affected by phase errors in quantum interference). For the same reason, the similarity for indistinguishable pairs of photons is reduced due to the limited accuracy of photon wavefront shaping via SLM. Indeed, shaping circuits with $N$ outputs is fundamentally limited by the capacity $M$ of MMF: as $N$ gets to $M$, control over TM coefficients becomes more difficult [27]. Also, for larger numbers of detectors the similarity decreases because the coincidence distribution becomes more noisy (see Fig. 4).

To conclude, we present an approach to implementing high-dimensional reconfigurable quantum circuits using wavefront shaping and mode mixing in the MMF with a SPAD array as a detector. We demonstrate the feasibility of the presented approach by implementing a complex linear network for two-photon interference [18,28]. We measure the number of counts and the two-photon correlations between all the output pairs within a 10 ns time-window using a time-tagging SPAD array [29,30], thus advancing towards scalable detection schemes beyond previously proposed solutions [12,14]. However, like all SPAD arrays SPAD23 is prone to cross-talk, which occurs when a photon detected by one of the array's detectors is simultaneously counted by a neighboring detector [21,29].

While the probability of cross-talk is low (approximately 0.1%), it affects the number of coincidences measured in our experiment but not the number of single photon counts [21]; thus we employed a proper subtraction procedure (Supplement 1). The current technical limitations are the number of available photons and detection efficiency (20%), preventing us from studying high-dimensional linear networks applied to multi-photon states $\mathcal{L}$ [31,32], as well as detector cross-talk [21], which affect coincidences between detectors located close to each other thus reducing the measured similarity of the states. However, the scalability and programmable nature of the presented approach make it promising for applications in quantum information processing, especially in the perspective of using more photons and detectors to test different boson sampling protocols which can overcome the capabilities of existing classical information processing schemes [31].

**Funding.** European Research Council (SMARTIES-724473, SQIMIC-101039375); Fundacja na rzecz Nauki Polskiej (MAB/2019/12, First Team POIR.04.04.00-00-3004/17-00).

**Acknowledgment.** We would like to thank Saroch Leedumrongwatthanakun for fruitful discussions and initial guidance with the setup.

**Disclosures.** C. B.: PI Imaging Technology SA (I, S); I. M. A.: PI Imaging Technology SA (I, E); E. C.: Fasttree3D SA (I, S) and PI Imaging Technology SA (I, S); S. G.: LightOn SA (C).

**Data availability.** Data underlying the results presented in this paper may be obtained from the authors upon reasonable request.

**Supplemental document.** See Supplement 1 for supporting content.

## REFERENCES

1. R. Fickler, R. Lapkiewicz, W. N. Plick, *et al.*, Science **338**, 640 (2012).
2. M. Arndt and K. Hornberger, Nat. Phys. **10**, 271 (2014).
3. A. Aspect, P. Grangier, and G. Roger, Phys. Rev. Lett. **47**, 460 (1981).
4. M. A. Broome, A. Fedrizzi, S. Rahimi-Keshari, *et al.*, Science **339**, 794 (2013).
5. N. H. Valencia, S. Goel, W. McCutcheon, *et al.*, Nat. Phys. **16**, 1112 (2020).
6. A. M. Childs, Phys. Rev. Lett. **102**, 180501 (2009).
7. M. Barbieri, PRX Quantum **3**, 010202 (2022).
8. N. Aslam, H. Zhou, E. K. Urbach, *et al.*, Nat. Rev. Phys. **5**, 157 (2023).
9. A. Schreiber, A. Gábris, P. P. Rohde, *et al.*, Science **336**, 55 (2012).
10. A. Peruzzo, M. Lobino, J. C. F. Matthews, *et al.*, Science **329**, 1500 (2010).
11. T. Kitagawa, M. A. Broome, A. Fedrizzi, *et al.*, Nat. Commun. **3**, 882 (2012).
12. S. Leedumrongwatthanakun, L. Innocenti, H. Defienne, *et al.*, Nat. Photonics **14**, 139 (2020).
13. D. J. Brod, E. F. Galvão, A. Crespi, *et al.*, Adv. Photonics **1**, 034001 (2019).
14. H. Defienne, M. Barbieri, I. A. Walmsley, *et al.*, Sci. Adv. **2**, e1501054 (2016).
15. A. Cavaillès, P. Boucher, L. Daudet, *et al.*, Opt. Express **30**, 30058 (2022).
16. J. G. Titchener, A. S. Solntsev, and A. A. Sukhorukov, Opt. Lett. **41**, 4079 (2016).
17. S. R. Huisman, T. J. Huisman, T. A. W. Wolterink, *et al.*, Opt. Express **23**, 3102 (2015).
18. P. M. Preiss, R. Ma, M. E. Tai, *et al.*, Science **347**, 1229 (2015).
19. "SPAD23 documentation," https://piimaging.com/product-spad23.
20. C. K. Hong, Z. Y. Ou, and L. Mandel, Phys. Rev. Lett. **59**, 2044 (1987).
21. G. Lubin, R. Tenne, I. M. Antolovic, *et al.*, Opt. Express **27**, 32863 (2019).
22. A. Ghezzi, A. Farina, A. Bassi, *et al.*, Opt. Lett. **46**, 1353 (2021).
23. I. M. Antolovic, C. Bruschini, and E. Charbon, Opt. Express **26**, 22234 (2018).
24. S. M. Popoff, G. Lerosey, R. Carminati, *et al.*, Phys. Rev. Lett. **104**, 100601 (2010).
25. D. Loterie, S. Farahi, I. Papadopoulos, *et al.*, Opt. Express **23**, 23845 (2015).
26. A. Y. Vlasov, Laser Phys. Lett. **14**, 103001 (2017).
27. I. M. Vellekoop and A. P. Mosk, Opt. Lett. **32**, 2309 (2007).
28. T. A. W. Wolterink, R. Uppu, G. Ctistis, *et al.*, Phys. Rev. A **93**, 053817 (2016).
29. C. Bruschini, H. Homulle, I. M. Antolovic, *et al.*, Light Sci. Appl. **8**, 87 (2019).
30. E. Slenders, M. Castello, M. Buttafava, *et al.*, Light Sci. Appl. **10**, 31 (2021).
31. H. Wang, J. Qin, X. Ding, *et al.*, Phys. Rev. Lett. **123**, 250503 (2019).
32. J. Wang, S. Paesani, Y. Ding, *et al.*, Science **360**, 285 (2018).

128.178.116.117 on 2024-07-04 10:08:367